LAWRENCE
LIVERMORE
NATIONAL
LABORATORY

UCRL-JRNL-218859

Simulating Thermal Explosion of Octahydrotetranitrotetrazine-based explosives: Model Comparison with Experiment

J. J. Yoh, M. A. McClelland, J. L. Maienschein, A. L. Nichols, C. M. Tarver

February 10, 2006

Journal of Applied Physics

Disclaimer

Simulating thermal explosion of octahydrotetranitrotetrazine-based explosives: Model comparison with experiment

Jack J. Yoh

School of Mechanical and Aerospace Engineering

Seoul National University, Seoul 151-742, Korea

Matthew A. McClelland, Jon L. Maienschein, Albert L. Nichols, and Craig M. Tarver

Energetic Materials Center

Lawrence Livermore National Laboratory,

Livermore, CA 94551

(Dated: January 20, 2006)

Abstract

We compare two-dimensional model results with measurements for the thermal, chemical and mechanical behavior in a thermal explosion experiment. Confined high explosives are heated at a rate of 1 °C per hour until an explosion is observed. The heating, ignition, and deflagration phases are modeled using an Arbitrarily Lagrangian-Eulerian code (ALE3D) that can handle a wide range of time scales that vary from a structural to a dynamic hydro time scale. During the pre-ignition phase, quasi-static mechanics and diffusive thermal transfer from a heat source to the HE are coupled with the finite chemical reactions that include both endothermic and exothermic processes. Once the HE ignites, a hydro dynamic calculation is performed as a burn front propagates through the HE. Two octahydrotetranitrotetrazine (HMX)-based explosives, LX-04 and LX-10, are considered, whose chemical-thermal-mechanical models are constructed based on measurements of thermal and mechanical properties along with small scale thermal explosion measurements. The present HMX modeling work shows very first violence calculations with thermal predictions associated with a confined thermal explosion test. The simulated dynamic response of HE confinement during the explosive phase is compared to measurements in larger scale thermal explosion tests. The explosion temperatures for both HE's are predicted to within 1 °C. Calculated and measured wall strains provide an indication of vessel pressurization during the heating phase and violence during the explosive phase.

PACS numbers: 82.33.Vx, 46.15.-x, 47.40.-x

I. INTRODUCTION

In the energetic materials community, there is an interest in using computer simulations to reduce the number of experiments for weapons design and safety evaluation. One area of success in modeling and simulation is the characterization of munitions exposed to extreme conditions, such as shocks and detonations [1–3]. Hydrocodes, which are designed to simulate the high-frequency response involving initiation and propagation of shocks and detonations, have been used extensively by the energetic materials community [4–9].

On the other hand, models and numerical strategies are still being developed for the heating of energetic materials until reaction (cookoff) [10–14]. The Navy is interested in the behavior of munitions in shipboard fires to help with the design of storage systems and the development of fire fighting strategies. In these fires, time scales for behavior can range from days to microseconds. During the relatively slow heating phase, the response of an energetic materials system is paced by thermal diffusion and chemical decomposition, while the mechanical response is essentially a quasi-static process. As the decomposition reactions accelerate, heat is generated faster than it can diffuse. Product gases are formed and the resulting pressure rises accelerate the energetic and containment material response. The resulting thermal explosion can range in violence from a pressure rupture to a detonation. A number of investigators have modeled slow cookoff experiments. The explosion times for HMX- and tiaminotrinitrobenzene (TATB)-based explosives subjected to varying confinement and thermal environments were calculated in [15]. In [16], the authors improved thermal decomposition models for HMX-based plastic bonded explosives and attained reasonable predictions for ignition time using the thermal-chemical code, Chemical TOPAZ. These thermo-chemical models were expanded to include hydro effects, and the earlier models were evaluated against small-scale tests (see [11, 17, 18]). It was recognized that the models required further development and needed to be benchmarked against well-instrumented cookoff experiments (see [19–21]). More recent modeling efforts have focused on wall strain rates as a measure of cookoff violence. Erikson *et al.* [22] used a suite of codes to model the two separate phases of the cookoff process. The information obtained from their pre-ignition calculation was used to initialize the post-ignition simulation for predicting the wall expansion. In [14], cyclotrimethylenetrinitramine (RDX)-based explosives cookoff models were compared against carefully instrumented experiments, and the violence

predictions were made with reasonable accuracy.

The process of cookoff is not separated into two regimes in this work. Instead, a single calculation is performed for the heating, ignition, and explosive phases of cookoff. Coupled thermal, mechanical, and chemical models are used during all of these stages to account for effects such as chemical decomposition, burning, thermal expansion, and the closing of gaps. It is seen that the modeling of thermal explosions requires computational tools and models that can handle a wide variety of physical processes and time scales.

We consider the explosives LX-04 and LX-10 which have an HMX base [23]. The LX-04 has a nominal composition of 85% HMX and 15% Viton by weight, and the composition of LX-10 is 95% HMX and 5% Viton. The selection of these explosives allows us to investigate a range of HMX contents with simulations and experiments.

In this paper, we investigate the response of confined HMX-based materials in the Scaled Thermal Explosion Experiment (STEX). We use the ALE3D models to calculate temperature fields, the time to explosion, and strain of the vessel wall during the heating, ignition, and explosive phases of the experiment. A numerical approach involving variable mass-scaling allows the calculation of coupled thermo-chemical-mechanical results over the widely varying time scales associated with the heating and explosive processes [24, 25]. In all cases, we have performed mesh refinement analysis to help assess the accuracy of the results. Model simulations are compared with measurements from thermocouples and strain gauges.

II. SCALE THERMAL EXPLOSION EXPERIMENT (STEX)

In order to provide a database to test models, the STEX is designed to quantify the violence of thermal explosions under carefully controlled conditions [19]. The cylindrical test, shown in Fig. 1, is designed to provide ignition in the central region of the cylinder. The confinement vessel consists of two types of tubes; a 4130 steel tube and AerMet 100 with heavily reinforced end caps which confine the decomposition gases until the tube wall fails. A length to diameter ratio of 4:1 is used for which the ID is 5.08 cm for 4130 tube and 4.49 cm for AerMet 100, and the interior length is 20.3 cm. The wall thickness for LX-04 was 0.4 cm, while it was 0.3 cm for LX-10, giving an approximate minimum confinement pressure of 200 MPa for both cases. Ullage (air space) was included to allow for expansion of the HE without bursting the vessel prior to ignition. The total ullage that is present in

the vessel was 7% for LX-04 and 8.66% for LX-10.

A feedback control system is used to adjust three radiant heaters to control the wall temperature at location no. 1 of Fig. 1(b). The thermocouples at location nos. 2 and 3 on the end caps are controlled with separate control loops. The wall thermocouple temperature is increased at 1 °C/h until explosion. The lower and upper thermocouples are maintained at 4 and 9 °C, respectively, below the wall temperature to provide for ignition near a plane half way between the two end caps. A probe with 5 thermocouples is used to monitor the internal temperature of the HE (see Fig. 1(b)). Two hoop strain gauges were used to measure the radial expansion of the tube at the axial midplane.

III. MODELS FOR HMX-BASED EXPLOSIVES

In this model, the solid explosive decomposes volumetrically as it is heated to generate product gases (see Fig. 2(a)). These reactions accelerate to a point at which the HE ignites and burns. A burn front then moves as a sheet away from the ignition point (see Fig. 2(b)). Partially decomposed HE is converted to products as the burn front propagates. The product gases pressurize the vessel and drive the wall outward.

The decomposition of the two HMX-based explosives is modeled by four-step, five-species chemical kinetics reported in [16, 26]. The mechanical models for the solid chemical constituents use linear elastic-plastic solids with constant elastic modulus. The steel model includes strain hardening, while the HMX is taken to be perfectly plastic above yielding point. A polynomial expression is used for the equations of state. The gaseous products are treated as no-strength materials with gamma-law equations of state. The thermal conductivity for the HE solid species is taken to be constant, whereas the effects of temperature are included for the gaseous species. The air in the gaps between the HE and the steel case is described with a gamma-law model.

A. Chemical model

The four-step, five-species reaction mechanism for HMX is

$$\mathrm{A} \rightarrow \mathrm{B}, \quad r_1 = Z_1 \exp(-E_1/RT)\,\rho_{\mathrm{A}} \tag{1}$$

$$\mathrm{B} \rightarrow \mathrm{C}, \quad r_2 = Z_2 \exp(-E_2/RT)\,\rho_{\mathrm{B}} \tag{2}$$

$$\mathrm{C} \rightarrow \mathrm{D}, \quad r_3 = Z_3 \exp(-E_3/RT)\,\rho_{\mathrm{C}} \tag{3}$$

$$\mathrm{D} \rightarrow \mathrm{E}, \quad r_4 = Z_4 \exp(-E_4/RT)\,\rho_{\mathrm{D}}^2 \tag{4}$$

$$\tag{5}$$

where A and B are solid species (β- and δ-phase HMX), C is solid intermediate, D and E are intermediate and final product gases, respectively. Here r_i is the mass reaction rate, Z_i is the frequency factor, and E_i is the activation energy for reaction i. Also ρ_j is the mass concentration for species $j = A, B, C, D, E$.

The mechanism for Viton is a single-step, endothermic reaction:

$$\mathrm{Viton}_{solid} \rightarrow \mathrm{Viton}_{gas}, \quad r_1 = Z_1 \exp(-E_1/RT)\,\rho_{\mathrm{Viton}_{solid}} \tag{6}$$

The rate parameters in the above mechanisms for LX-04 and LX-10 are adjusted to fit One-Dimensional-Time-to-Explosion (ODTX) measurements [27]. The values are given in Table I.

The time-to-ignition measurements are made using a standard ODTX apparatus in which the outer surface of a 1.27 cm diameter HE sphere is suddenly increased to a specified temperature. The time to explosion is the time elapsed from the start of heating until confinement failure. The measured and calculated ODTX results for LX-04 and LX-10 are shown in Figs. 3 and 4, respectively. The ODTX measurements for both explosives include samples from the lots of LX-04 and LX-10 used in the larger scale STEX tests. The model includes chemical reaction and thermal transport without material motion. The model provides a good description of the measurements which exhibit some scatter.

After the chemical reactions have progressed significantly into the faster regime of cookoff in which changes are occurring on the time scale of the sound speed, a switch is made to a burn front model in which reactants are converted completely to products in a single reaction step. The burn front velocity, V is assumed to be a pressure-dependent function, and it takes the form

$$V = a\,P^n \tag{7}$$

where V is in mm/s and P is in MPa.

This change in models is made for several reasons. First the Arrhenius models described above may not apply at the elevated temperatures and pressures of the burn process. The burn rate model is more useful since it can employ measured burn rates as described below. Finally, the computational effort required for the Arrhenius model is prohibitively large as a result of the fine mesh spacing and small time steps required to model the narrow burn front. In contrast, solutions for the burn rate model can be obtained with practical amounts of computation time.

Fig. 5 shows one straight line and a curved line that represent the burn rate measurements. The burn rates are measured using the LLNL High Pressure Strand Burner [28]. A strand of explosive (0.64 cm D x 5.7 cm L) is placed in a high pressure vessel, and is ignited at one end. Wires placed in the sample track the progress of the burn while pressure measurements are made.

B. Constitutive model at high-strain rate

The steels are taken to be Steinberg-Guinan materials that incorporate an equation of state (EOS) and expressions for the shear modulus μ and yield strength Y. The steel model includes strain hardening, while the HE is taken to be perfectly plastic above the yield point.

The expression for the EOS of the unreacted explosive follows a 7-term polynomial in the form of

$$P(\xi) = a_0 + a_1\xi + a_2\xi^2 + a_3\xi^3 + (b_0 + b_1\xi + b_2\xi^2)\rho_0 c_v(T - T_0) \tag{8}$$

where the volumetric compression is defined $\xi = \rho/\rho_0 - 1$. Thus, a single EOS is used to represent behavior involving slow heating and the explosive process.

For the HE's, we set $a_0 = b_2 = 0$ and $b_0 = b_1$. The parameters, a_1, a_2, a_3, and b_0 were adjusted using a nonlinear regression procedure to provide a best fit of the measured thermal expansion, heat capacity, sound speed, and the unreacted shock Hugoniot (see [10]). All measurements are for the sample of this study, except for the shock Hugoniot. heat capacity, sound speed, and unreacted shock Hugoniot. In some cases, these properties were constructed from constituent measurements using mixing rules.

The EOS of the 4130 steel follows a 7-term polynomial as in the unreacted HE case. As

for AerMet 100, we use the Gruneisen EOS, where the pressure is defined as:

$$P = \begin{cases} \frac{\rho_0 c_0^2 \mu \left[1+\left(1-\frac{\Gamma_0}{2}\right)\mu - \frac{a}{2}\mu^2\right]}{1-(S_1-1)\mu - S_2\frac{\mu^2}{\mu+1} - S_3\frac{\mu^3}{(\mu+1)^2}} + (\Gamma_0 + a\mu)E, & \text{for } \mu > 0 \\ \rho_0\, c_0^2 \mu + (\Gamma_0 + a\mu)E, & \text{for } \mu < 0 \end{cases} \tag{9}$$

where the compression μ is given by $\mu = \rho/\rho_0$.

The model chemical components (C, D) are treated as no-strength materials with gamma-law equations of state,

$$P = (\gamma - 1)\,\rho\, c_v\, T \tag{10}$$

This type of EOS provides an approximate description for the relatively low confinement pressures (< 10 kbar) of thermal explosion tests. The value γ is adjusted using a pressure of 1 kbar, a temperature of 2000 °C, and density and heat capacity c_v determined from the thermo-chemical equilibrium computer code, Cheetah 3.0 [29] for the final product gases. A summary of the adjusted parameters for the current equations of state is given in Table II.

The shear modulus, μ, and yield stress, Y of both steels are assumed to vary with temperature, but are not strain-rate dependent. Strain hardening is present for the steel, but not for the solid HE constituents (see Table III and IV.)

$$\mu(P, \eta, T) = \mu_0 \left[1 + b\frac{P}{\eta^{1/3}} - h(T - 300)\right] \tag{11}$$

$$Y(P, \eta, \bar{\epsilon}^p, T) = Y_0[1 + \beta(\bar{\epsilon}^p + \bar{\epsilon}_0^p)]^n \frac{\mu}{\mu_0} \tag{12}$$

with the maximum work hardening given by

$$Y_0[1 + \beta(\bar{\epsilon}^p + \bar{\epsilon}_0^p)]^n \leq Y_{\max}. \tag{13}$$

In these expressions, we have

$$\eta = \frac{\rho}{\rho_0}$$

$$\bar{\epsilon}^p = \int \dot{\bar{\epsilon}}^p\, dt$$

$$\dot{\bar{\epsilon}}^p = \sqrt{\frac{2}{3}\left((\dot{\epsilon}_1^p - \dot{\epsilon}_2^p)^2 (\dot{\epsilon}_2^p - \dot{\epsilon}_3^p)^2 (\dot{\epsilon}_3^p - \dot{\epsilon}_1^p)^2\right)}$$

where the directional components of plastic strain rates are noted as $\dot{\epsilon}_i^p$. The subscript 0 refers to the reference state ($T = 300$ °K, $P = 0$, $\epsilon = 0$). In general, we set $\bar{\epsilon}_0^p$ to zero for

each material. When melting occurs ($T \geq T_m$), the material model assumes zero strength and effectively $\mu = Y = 0$.

In [30], the authors showed that for materials that do not exhibit strain-rate dependency, Y is expected to be proportional to μ; that is Y/μ is a constant. Generally, this ratio decreases with temperature at a rate directly related to $\dot{\epsilon}$, $\dot{\epsilon} \geq 10^5\,\mathrm{s}^{-1}$, where a weaker temperature dependence is observed.

It is important to note that μ and Y drop to zero upon melting and that the above expressions are valid for the solid phase where $T < T_m$. The melt temperature T_m is given by a modified Lindemann melting law which is given elsewhere [30].

The present strength model of Steinberg-Guinan predicts that the shear modulus decreases with temperature, dropping abruptly to zero at $T \geq T_m$. For further detail on the model, readers are referred to [30, 31].

The constants $b, h, \beta, n, \mu_0, Y_0$ and $Y_{\max}$ are shown in Table V. The values for μ_0 and Y_0 were based on measurements. It is noted that since the strength of the solid HE constituents is small, the behavior is similar in many ways to that of a hydrostatic liquid. A more complex viscoelastic model would be a better choice for all of the solid HE constituents. The LX-04 has 15% and the LX-10 has 5% plastic binder. These materials would be expected to exhibit viscous behavior at low strain rates during the heating phase and more elastic behavior at high strain rates. The impact of the model choices are being explored in this and other investigations.

C. Thermal model

The time-dependent thermal transport model includes the effects of conduction, reaction, convection, and compression. The constant-volume heat capacity is constant for each reactant consistent with the Steinberg-Guinan model. The thermal conductivities of the solid species A, B, and C are taken to be constant, whereas the effects of temperature are included for the gaseous species. The thermal properties for materials A, B, and C are listed in Table II and use available measured values for LX-04 and LX-10. The heat capacity, c_v, for gases C and D is assigned the same constant-volume value used in the gamma-law model. The temperature-dependent thermal conductivity is estimated at 1 kbar and T = 2000 °C using Bridgmann's equation [32] for liquids in which the sound velocity is calculated using

results from Cheetah.

IV. MODELING DETAILS AND NUMERICAL STRATEGY

A. ODTX tests

The ODTX system is modeled using the ALE3D code; the problem is spherically symmetric and one-dimensional in the r-direction. The mesh has one row of 50 elements in the shape of a 'piton,' running from the center of the half-inch sphere to the outer boundary at $r = 0.635$ cm (see Fig. 6). The center axis of the piton is the x-axis. The vertex of the piton is flattened so that the mesh can be constructed from 8-noded hexahedral brick elements. The full domain is then a sphere with a small hole in the center. A step thermal boundary condition is applied at the outer end of the mesh. The decomposition rate accelerates and the calculation continues until the time step size decreases to a user-specified value. This time is taken to be the time to explosion.

B. STEX

Fig. 7 shows one and two-dimensional modeling domains for a STEX test. A wedge slice is taken from the center line of the STEX system shown in the right image. This one-dimensional wedge represents an axisymmetric section of the STEX system in which variations occur only in the radial direction. This approach is taken to minimize the number of three-dimensional zones needed to represent an axisymmetric domain. The boundaries at two planes of constant θ and two planes of constant z are rigid slip surfaces. In the experiment [33], the HE, nominally 5.08 cm diameter is encased in either 0.1 cm or 0.4 cm thick steel cylinder. Gap volumes of 7 and 8.66% for LX-04 and LX-10, respectively, are located at the outside radius of the HE in both 1D and 2D models.

The three heaters were modeled as uniform heat flux surfaces on the tube wall and top and bottom surfaces for the end caps (see Fig. 1). Model Proportional-Integral-Derivative (PID) controllers were used to keep the three control temperatures near their set-point values. Expressions for heat transfer coefficients were applied at all outward facing surfaces of the capped tube to account for the effects of free convection and thermal radiation heat losses to the surroundings [34]. A more refined boundary-layer expression for heat transfer

is used at the tube wall to account for spatial variations resulting from the rising warm air. The heat transfer is high near the lower end of the tube wall and decreases up the tube wall as the boundary layer of warm air forms and increases in thickness.

The cookoff simulation starts with a gradual increase of the set-point temperature at location no. 1 in Fig. 1(b) to 130 °C, followed by a hold for 5 hours, and then an increase at a rate of 1 °C/h until cookoff. The upper (no. 2) and lower (no. 3) control thermocouples were kept a few degrees lower than the tube control TC in an effort to place the ignition point in the center of the HE. As the HE is heated, it thermally expands to fill in the gap. At a temperature above 130 °C, exothermic decomposition begins and eventually ignition occurs near the midplane of the system. On a time scale of microseconds, the propagation of flame through the HE causes the temperature and pressure to rise, and ultimately causes a break in confinement.

In the simulations, two different mesh resolutions ($\Delta x, \Delta x/2$) are considered. In the base case (Δx), there are 12 elements across the HE in the radial direction, 3 elements across the steel wall. The air/HE interface is not tracked explicitly, and zones with both air and HE have properties determined by the mixing rule discussed next.

C. Numerical strategies for dynamic gaps

In real systems, there are gaps present between the HE sample and its case. Whether the presence of gaps is by design or not, its effect on the cookoff violence is believed to be significant. The ALE3D code has two ways of modeling gaps. The first way uses a standard sliding contact algorithm that makes use of the concept of master-slave surfaces. Here, finite element boundaries coincide with phase boundaries, and the gap surfaces are explicitly 'tracked.' The second way of treating gaps is the mixed element approach that we use in this work. Interfaces pass through the middle of mixed elements that do not necessarily move with the interface. The interface is resolved on the length scale of this element. Although less accurate, this approach avoids mesh tracking and entanglement problems. The mixed-element approach can provide results of satisfactory accuracy with careful handling.

The mixing rules for mechanical behavior are particularly important for gaps that close. The algorithms of this study were devised with the assumption that the HE/air interface

is parallel to the case wall, which is generally valid except at corners of the explosive. Mechanical properties in the mixed zone are weighted in favor of the air in the gap. In the vicinity of this interface, strains normal to the interface are very small for the HE and relatively large for the air in the gap.

D. Time integration method, mass scaling, and transition to burn

The equations of mass, momentum, energy, and chemistry are solved on the long time scale of the heating phase and on the short time scale of the thermal runaway phase in a single simulation. The momentum equation is integrated explicitly during both the slow and fast phases. In order to provide computationally feasible step sizes, the method of variable mass scaling [35] is applied during the slow heating phase. The density is increased in the momentum equation to reduce the sound speed and allow larger step sizes consistent with the Courant condition. However, if the time step size and material density are too large, spurious fluctuations, characteristic of a simple harmonic oscillator, appear. Thus, a tradeoff is required between numerical efficiency and accuracy. In practice, the time step size is fixed during the slow heating phase with the density calculated from the Courant condition. As the mesh is refined, the time-step size is reduced to keep the mass scaling and the sound speed at nearly constant values.

During the transition phase in which the decomposition reactions are accelerating, the time step size is reduced to meet error specifications for the calculation of thermal and composition fields. At the same time, the artificial density is reduced following the Courant condition until the physical value is obtained. Fig. 8 illustrates the size of time steps during the last three hours before ignition. Plotted on the y-axis are the actual time-step sizes recorded from a standard simulation. As mass is removed from the system, the size of time steps changes from $10^{8}\,\mu$s to $10^{-7}\,\mu$s. An approximate step size decrease on the order of $10^{14}\,\mu$s magnitude is noted during this transition.

When the HE reaches a user-specified temperature at which ignition occurs, the Arrhenius kinetics expression is replaced by a burn model. A level-set method is used in the modeling of the advancing burn front. The equation

$$\phi_t + \boldsymbol{V}(P) \cdot \nabla\phi = 0 \tag{14}$$

keeps track of the front location as the zero level of ϕ. The pressure-dependent burn velocity $\boldsymbol{V}$ is a single valued vector $(V, V, V)^{\top}$. In the most general frame of level sets, ϕ starts out as the signed distance function, is advected by solving Eqn. 14, and then is reinitialized using a distance renormalization procedure discussed in [25].

We use the Backward Euler method for the integration of the thermal equations and reaction kinetics during the heating, and transition phases. During the slow heating phase, the time step size is the value selected for the integration of the hydrodynamic equations. A switch is made to an explicit method when the time step size is a user-specified multiple of the Courant time step size calculated with no mass scaling.

V. RESULTS

A. One-dimensional analysis and model verification

The simplified geometry shown in Fig. 7(a) is used to verify the HE models and check for numerical accuracy. Many of the important features of the thermal explosion models can be efficiently explored with quantitative predictions for the time to explosion and qualitative simulations for the vessel wall expansion as described below. Comparisons of model calculations against the experimental records will be described in the two-dimensional analysis section.

The system was heated using the temperature profile described above for control thermocouple no. 1 of Fig. 1(b). The explosive expands radially into the gap, decomposes, and ignites near the symmetry axis. The ignition temperature based on the control TC no. 2 of Fig. 7(a) is calculated to be 189 °C for LX-04 and 190 °C for LX-10 (see Table VI). The Δx mesh with 12 zones in the radial direction was used for the calculations. More refined meshes gave the same explosion temperatures to within 1 °C.

After the ignition, the burn front advances outward into the relatively cold solid explosive. The resulting high pressure product gases drive the steel case outward. Calculated results for the wall hoop strain at location no. 2 of Fig. 7(a) are shown in Figs. 9 and 10 for the one-dimensional STEX model. For comparison, the theoretical thermal expansion of an empty steel vessel is shown in the same plot. The system for LX-04 has 7% gap between the HE and the steel plate with thickness of 0.4 cm. For LX-10 system, the gap size is 8.66%

and the plate thickness is 0.3 cm. The HE-vessel and empty vessel results should coincide as the temperature increases until the HE expands to fill the vessel or decomposition gases pressurize the vessel. Note that the coefficients of thermal expansion for the explosives are 5X greater than the steels (see Tables II and III). The estimated time of contact at which inert HE fills the gap and starts pushing on the steel wall is approximately 35 hours for both LX-04 and LX-10. Since the solid HE undergoes chemical decomposition and the decomposition gases pressurize the vessel, the overall strain values are greater than the analytical expansion of the steel vessel alone. The effects of mesh refinement on the strain curves were not pursued due to the simplicity of the problem set up.

B. Two-dimensional analysis

Two dimensional simulations are performed for the STEX system shown in Figs. 1(b) and 7(b) for LX-04 and LX-10. This system is assumed to be axisymmetric, and a cylindrical wedge was selected for the calculation domain. In Figs. 11 and 12, calculated temperatures of the STEX system are plotted versus time, along with measured curves. The measured and calculated temperatures are shown at an internal location (no. 6 in Fig. 1(b)) and the control location (no. 1 in Fig. 1(b)). The predicted and measured internal temperature curves are in good agreement for LX-04, and the predicted explosion temperature (TC no. 1) of 189 °C agrees very well with the experimental value of 190 °C (see Table VI). For LX-10, the predicted curve nearly reproduces the measurement with only a slight discrepancy in the explosion temperature (e.g. predicted at 182 °C versus measured at 181.5 °C.) The minor differences between the model and measured results are likely the result of inaccuracies in the chemical kinetics models. Despite this discrepancy, both the model and experiment give a lower cookoff temperature for LX-10 than LX-04. Studies were conducted to assess the accuracy of the calculations and the reproducibility of the measurements. The model simulations were repeated with the refined meshes and are numerically accurate to less than a degree. Thus, the model results are numerically accurate and the measurements seem to be reproducible.

In Figs. 13 and 14, calculated vessel wall hoop strains for the LX-04 and LX-10 STEX systems are shown with the measurements over the duration of the tests. Until a few hours before the ignition point, these results confirm the accuracy of the hoop strain calculations

and the polynomial EOS for the 4130 steel and Gruneisen EOS for AerMet 100. Near the ignition point, decomposition gases pressurize the vessel, and calculated strains are greater than the measurements.

The calculated wall-hoop strain for both cases is shown for the base-line case $(\Delta t, \Delta x)$ and a case $(\Delta t/2, \Delta x/2)$ in which the time-step size is also reduced by a factor of two. This decrease in Δt is implemented during the heating phase and reduces the mass scaling. (Note that the value for Δt is not decreased below the Courant limit.) These simulation results show oscillations, and are generally higher than the measurements and the analytical empty-vessel results. Consequently, calculated pressures within the HE are higher than pressures inferred from strain measurements. Mass scaling and mixed materials modeling of gaps contribute to these artificially high pressures as described below. Near the ignition point there is additional pressurization resulting from the decomposition gases. Note that the deformation of the explosives contributes little to the high pressures since both explosives have low strength and deform easily as they thermally expand and fill the steel vessel.

As Δx and Δt are reduced, the calculated strain curves are approaching the empty-vessel results. Mesh refinement provides a better representation of the HE/air interface near the vessel wall, and a smaller time-step size decreases the mass scaling. Although the results do not show complete convergence with either the mesh or time-step size, they do provide an approximate description of the mechanical behavior during the heating and ignition phases.

It is useful to further consider the contribution of mass scaling to the numerical artifacts in the calculated strain curves. The large calculated strains are primarily the result of reduced sound speeds from mass scaling. The HE pressurizes the vessel before there is time for the explosive to expand upwards into the gap region near the top of the vessel. If the mass scaling is reduced, the upward expansion occurs faster, there is less pressurization, and the tube wall strains are reduced. The spurious oscillations are similar to those observed for a simple harmonic oscillator in which the motion of the high mass material is guided by the restoring force of material elasticity. As the mass scaling is reduced, the amplitude decreases and the frequency of the oscillations increase. It is important to minimize these errors since the state of the system prior to ignition can have a strong influence on the violence of the expansion.

VI. CONCLUSIONS

A numerical investigation was performed to validate the experimental results for the thermally-induced explosion of the HMX-based explosives LX-04 and LX-10. The explosives were heated in steel vessels at 1 °C/h until reaction. ALE3D models were employed to represent the coupled thermal, chemical, and mechanical behavior through the heating, ignition, and explosive phases. For the solid explosives, we use a polynomial equation of state and an elastic-plastic model. Model parameters were obtained from measurements of thermal and mechanical properties at conditions relevant to both the slow heating and explosive phases of cookoff. All of the gas species are taken to have gamma-law equations of state. Multi-step reaction models are used to represent the chemical kinetics behavior of these materials during the slow heating stage. Model parameters were specified using measurements of the one-dimensional-time to explosion. After ignition, we employ a flame sheet model with a power-law expression for the burn front velocity. Model parameters are determined from measurements of burn velocity in strands of explosive. During the heating phase, an implicit method is employed for the integration of the thermal-chemical transport equations, and an explicit method with mass scaling is used for the hydrodynamic equations. A mixed materials method was used to model the gap between the HE and vessel wall, while a level-set method was utilized to model the propagation of the burn front.

Calculations for one-dimensional models of the thermal explosion experiments for LX-04 and LX-10 are useful since they provide an approximate model for the wall expansion, and an assessment of numerical accuracy. Two-dimensional calculations for the temperature fields and explosion temperature are in excellent agreement with thermocouple measurements for both LX-04 and LX-10. Since the majority of the explosion time is consumed during the heating phase, accurate decomposition kinetic schemes previously tuned from a series of ODTX tests made such precise thermal predictions viable. As for the mechanical response, it is much more difficult to obtain wall strains as close as the measurements by the current state of numerical techniques which cannot fully address energetic solid 'motions' during the slow heating phase. However, the presented violence calculation of HMX cookoff experiment is unique and has never been achieved by anyone else, yet, an improved numerical feature is suggested for future work. In particular, the implicit hydro method is preferred over the explicit approach during the slow decomposition process where the most critical changes in

the unreacted solid HMX takes place. Calculated wall motions exhibit oscillatory behavior and are larger than the measured values due to artificial pressure rises from mass scaling. An implicit method can provide less oscillatory result, and thus more accurate wall motions during heating phase. This is important for the consequential explosive phase calculation where ignition and initiation of HMX strongly influence violence.

Acknowledgments

The work was performed under the auspices of the U.S. Department of Energy by the University of California, Lawrence Livermore National Laboratory under Contract No. W-7405-Eng-48. Jack J. Yoh also aknowledges the support from the BK 21 Project through the Institute of Advanced Aerospace Technology at Seoul National University.

[1] Mair, H. U., 'Review: Hydrocodes for Structural Response to Underwater Explosions,' *Shock and Vibration*, **6**, pp. 81–96, 1999.

[2] McGlaun, J. M., and Yarrington, P., Asay, J. R., and Shahinpoor, M., (Eds.) High Pressure Shock Compression of Solids, *Large Deformation Wave Codes*, Springer-Verlag, 1993.

[3] Anderson, Jr., C. E., 'An Overview of the Theory of Hydrocodes,' *Int. J. Impact Engineering*, **5**, pp. 33–59, 1987.

[4] McGlaun, J. M., Thompson, S. L., and Elrick, M. G., 'CTH: a Three-dimensional Shock Wave Physics Code,' *Int. J. Impact Engineering*, **10**, pp. 351–360, 1990.

[5] Kothe, D.B., Baumgardner, J.R., Cerutti, J.H., Daly, B.J., Holian, K.S., Kober, E.M., Mosso, S.J., Painter, J.W., Smith, R.D., and Torrey, M.D., 'PAGOSA: a Massively-Parallel, Multi-Material Hydrodynamics Model for Three-Dimensional High-Speed Flow and High-Rate Material Deformation,' *Proceedings of the 1993 Simulation Multiconference on the High Performance Computing Symposium*, pp. 9–14, San Diego, CA, 1993.

[6] Stewart, D. S., Aslam, T., Yao, J., and Bdzil, J. B., 'Level-set Techniques Applied to Unsteady Detonation Propagation,' *Modeling in Combustion Science, Proceedings, Springer-Verlag*, pp. 352–369, Berlin, Germany, 1995.

[7] Yoh, J. J., 'Thermomechanical and Numerical Modeling of Energetic Materials and Multi-Material Impact,' Ph. D. thesis, Theoretical and Applied Mechanics, University of Illinois at Urbana-Champaign, 2001.

[8] Bourlioux, A., and Majda, A. J., 'Theoretical and Numerical Structure for Unstable Two-Dimensional Detonations,' *Combustion and Flame*, **90**, pp. 211–229, 1992.

[9] Oran, E. S., Boris, J. P., Young, T., Flanigan, M., Burks, T., and Picone, M., 'Numerical Simulations of Detonations in Hydrogen-Air and Methane-Air Mixtures,' *Proceedings of 18th Symposium on Combustion*, The Combustion Institute, 1981, pp. 1641–1649.

[10] McClelland, M. A., Maienschein, J. L., Nichols, A. L., and Yoh, J. J., 'Ignition and Initiation Phenomena: Cookoff Violence Prediction,' *Joint DoD/DOE Munitions Technology Development Program FY-02 Report*, UCRL-ID-103482-02, 2002.

[11] Nichols, A. L., Couch, R., McCallen, R. C., Otero, I., and Sharp, R., 'Modeling Thermally Driven Energetic Response of High Explosives,' *Proceedings of 11th International Detonation Symposium*, Snowmass, Colorado, pp. 862–871, 1998

[12] Yoh, J. J., and McClelland, M. A., 'Simulating the Thermal Response of High Explosives on Time Scales of Days to Microseconds,' *Proceedings of 13th APS SCCM Conference*, Portland, Oregon, 2003.

[13] Yoh, J. J., McClelland, M. A., Maienschein, and Wardell, J. F., 'Towards a Predictive Thermal Explosion Model for Energetic Materials,' *J. of Computer-Aided Materials Design*, **10**, pp175-189, 2005.

[14] Yoh, J. J., McClelland, M. A., Maienschein, J. L., and Tarver, C. M., 'Simulating Thermal Explosion of Cyclotrimethylenetrinitramine (HMX)-based Explosives: Model Comparison with Experiment,' *Journal of Applied Physics*, **97**, 083504, 2005.

[15] Chidester, S. K., Tarver, C. M., Green, L. G., and Urtiew, P. A., 'On the Violence of Thermal Explosion in Solid Explosives,' *Combustion and Flame*, **110**, pp. 264–280, 1997.

[16] Tarver, C. M., and Tran, T. D., 'Thermal Decomposition Models for HMX-based Plastic Bonded Explosives,' *Combustion and Flame*, **137**, pp50–62, 2004.

[17] Baer, M. R., Hobbs, M. L., Gross, R. J., and Schmitt, R. G., 'Cookoff of Energetic Materials,' *Proceedings of 11th International Detonation Symposium*, Snowmass, Colorado, Office of Naval Research, pp. 852–861, 1998.

[18] Matheson, E. R., Drumheller, D. S., and Baer, M. R., 'A Coupled Damage and Reaction Model for Simulating Energetic Material Response to Impact Hazards,' *Proceedings of APS SCCM Conference*, Snowbird, Utah, pp. 651–654, 1999.

[19] Wardell, J. F., and Maienschein, J. L., 'The Scaled Thermal Explosion Experiment,' in *Proceedings of 12th International Detonation Symposium*, San Diego, CA, Office of Naval Research, 2002.

[20] Atwood, A. I., Curran, P. D., Lee, K. B., Bui, D. T., and Boggs, T. L., *Proceedings of 12th International Detonation Symposium*, San Diego, FL, 2002.

[21] Sandusky, H. W., Chambers, G. P., Erikson, W. W., and Schmitt, R. G., *Proceedings of 12th International Detonation Symposium*, San Diego, CA, 2002.

[22] Erikson, W. W., and Schmitt, R. G., *Insensitive Munitions and Energetic Materials Technology Symposium*, Bordeaux, France, 8-10 Oct. 2001.

[23] Meyer, R., Kohler, J., and Homburg, A, *Explosives*, Wiley-VCH, New York, 1993.

[24] Belytschko, T., 'An Overview of Semidiscretization and Time Integration Procedures,' in *Computational Methods for Transient Analysis*, edited by T. Belytschko and T. J. R. Hughes, North-Holland, 1983, pp. 1–65.

[25] Sharp, R., and the ALE3D Team, *Users Manual for ALE3D*, Lawrence Livermore National Laboratory, Ver. 3.6.1, October 25, 2003.

[26] Tarver, C. M., 'Chemical Kinetic Modeling of HMX and TATB Laser Ignition Tests,' *Journal of Energetic Materials*, **22**, pp93-107, 2004.

[27] Catalano, E., McGuire, R., Lee, E. L., Wrenn, E., Ornellas, D., and Walton, J., 'The Thermal Decomposition and Reaction of Confined Explosives,' *Proceedings of 6th International Detonation Symposium*, Coronado, CA, Office of Naval Research, pp. 214–222, 1976.

[28] Maienschein, J. L., Wardell, J. F., DeHaven, M. R., and Black, C. K., 'Deflagration e of HMX-based explosives at high temperatures and pressures,' *Propellants Explosives Pyrotechnics*, **24**, 5, 287-95, 2004.

[29] Fried, L. E., and Howard, W. M., *Cheetah 3.0 Users Manual*, Lawrence Livermore National Laboratory, Livermore, CA, UCRL-MA-117541, 2001

[30] Steinberg, D. J., Cochran, S. G., and Guinan, M. W., 'A Constitutive Model for Metals Applicable at High-strain Rate,' *Journal of Applied Physics*, **51**, pp. 1498–1504, 1980.

[31] Gust, W. H., 'High Impact Deformation of Metal Cylinders at Elevated Temperatures,' *Journal of Applied Physics*, **53**, pp. 3568–3575, 1982.

[32] Bird, R. B., Stewart, W. E., and Lightfoot, E. N., *Transport Phenomena*, John Wiley & Sons, Inc., 1960, pp. 260–261.

[33] McClelland, M. A., Maienschein, J. L., Yoh, J. J., deHaven, M. R., and Strand, O. T., 'Measurements and ALE3D Simulations for Violence in a Scaled Thermal Explosion Experiment with LX-10 and AerMet 100 Steel,' *sumitted to Propellants Explosives Pyrotechnics*, 2006.

[34] Holman, J. P., *Heat Transfer*, McGraw-Hill, 1976, pp. 253–254.

[35] Prior, A. M., 'Applications of Implicit and Explicit Finite Element Techniques to Metal Forming,' *J. of Material Processing Technology*, **45**, pp. 649–656, 1994.

TABLE I: Chemical kinetics parameters for decomposition of LX-04 and LX-10.

Reaction step	$\ln Z_k$	E_k (kJ/g-mole-^{o}K)	q_k (J/g)
$HMX_A \rightarrow HMX_B$	48.13 s^{-1}	202.93	41.88 (endothermic)
$HMX_B \rightarrow HMX_C$	48.70 s^{-1}	220.64	209.38 (endothermic)
$HMX_C \rightarrow HMX_D$	37.80 s^{-1}	185.48	-808.21 (exothermic)
$HMX_D \rightarrow HMX_E$	28.10 cm^3/s-g	142.77	-6155.75 (exothermic)
$Viton_{solid} \rightarrow Viton_{gas}$	32.70 s^{-1}	161.48	5862.6 (endothermic)

TABLE II: Constitutive parameters of LX-04 and LX-10 (HMX and Viton).

Parameter	Units	HMX			Viton	
		Solid-β	Solid-δ	Gases	Solids	Gases
Density, ρ_0	kg/m^3	1865	1767	1865	1830	1830
Coeff. 7-term polynomial, a_0	GPa	0	0		0	
Bulk modulus, a_1	GPa	13.5	13.5		13.5	
Coeff. 7-term polynomial, a_2	GPa	82.2	81.1		82.2	
Coeff. 7-term polynomial, a_3	GPa	0	0		0	
Coeff. 7-term polynomial, b_0		0.933	1.052		0.933	
Coeff. 7-term polynomial, b_1		0.933	1.052		0.933	
Coeff. 7-term polynomial, b_2		0	0		0	
Thermal conductivity, k	W/m/°C	0.456	0.456	0.1034	0.226	0.4188
Specific heat, c_v	J/kg/°C	1190	1190	1422	1005	1131
Thermal expansion coeff., α	°C^{-1}	5.11×10^{-5} [a]	5.46×10^{-5} [a]		4.24×10^{-5} [a]	
Initial shear modulus, μ_0	GPa	4.2	4.2			
Initial yield strength, Y_0	GPa	2.1×10^{-3}	2.1×10^{-3}			
Gamma-law coefficient, γ				1.283		1.283

[a] $\alpha = \frac{b_0 \rho_0 c_v}{3 a_1}$.

TABLE III: Constitutive parameters of 4130 Steel.

Parameter	Units	4130 Steel
Density, ρ	$\mathrm{kg/m^3}$	7830
Coeff. 7-term polynomial, a_0	GPa	0
Bulk modulus, a_1	GPa	159
Coeff. 7-term polynomial, a_2	GPa	160
Coeff. 7-term polynomial, a_3	GPa	0
Coeff. 7-term polynomial, b_0		1.65
Coeff. 7-term polynomial, b_1		0.5
Coeff. 7-term polynomial, b_2		0
Thermal conductivity, k	$\mathrm{W/m/^oC}$	42.7
Specific heat, c_v	$\mathrm{J/kg/^oC}$	444
Thermal expansion coeff., α	$\mathrm{^oC^{-1}}$	1.21×10^{-5} [a]
Initial shear modulus, μ_0	GPa	77
Initial yield strength, Y_0	GPa	1.03
Gamma-law coefficient, γ		

[a] $\alpha = \frac{b_0 \rho_0 c_v}{3 a_1}$.

TABLE IV: Constitutive parameters of AerMet 100 Steel and air.

Parameter	Units	AerMet 100	Air (Void Gas)
Density, ρ	kg/m^3	7923	1.206
Sound speed ($U_s - u_p$ intercept), c_0	m/s	4534	
Linear $U_s - u_p$ coefficient, S_1		1.5	
Gruneisen gamma, Γ_0		1.84	
Correction to Γ_0, a		0.5	
Thermal conductivity, k	W/m/^{o}C	42.7	0.0257[a]
Specific heat, c_v	J/kg/^{o}C	444	707
Thermal expansion coeff., α	^{o}C^{-1}	1.21×10^{-5}[b]	
Initial shear modulus, μ_0	GPa	74.8	1.0×10^{-3}[c]
Poisson ratio, ν		0.302	
Initial yield strength, Y_0	GPa	1.56	1.0×10^{-4}[c]
Gamma-law coefficient, γ			1.4

[a](T,P)=(20 ^{o}C, 1 atm).
[b]$\alpha = \frac{b_0 \rho_0 c_v}{3 a_1}$.
[c]Modeled quantity for air gaps.

TABLE V: Constants in the equations of shear modulus and yield stress.

Material	μ_0 (GPa)	Y_0 (GPa)	$Y_{\max}$ (GPa)	β	n	b (GPa^{-1})	h (K^{-1})
HMX (β, δ)	4.2	2.1×10^{-3}					
Steel 4130	77.0	1.03	3.1	125	0.070	0.0	5.0505×10^{-4}
AerMet 100	74.8	1.0156	3.0	2	0.5	0.0	0.0

TABLE VI: Comparison of explosion temperatures.

Material	Experiment	Simulation
LX-04	190 °C	189 °C
LX-10	181.5 °C	182 °C

List of Figures

measurement. Δx mesh is used.

Fig. 13: Experimental and calculated hoop strain records from the slow heating to the thermal runaway phase for LX-04.

Fig. 14: Experimental and calculated hoop strain records from the slow heating to the thermal runaway phase for LX-10.

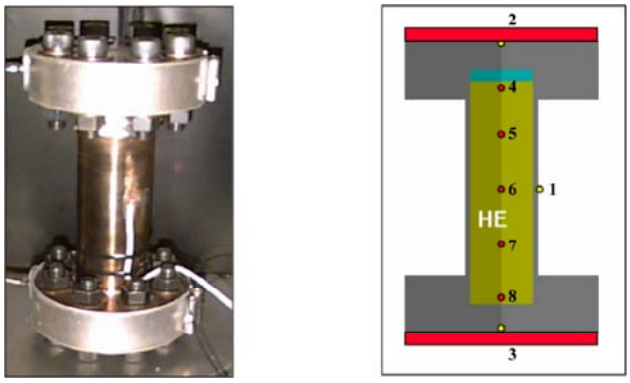

(a) (b)

FIG. 1: (a) Photograph of the STEX vessel. (b) Schematic of the ALE3D model domain.

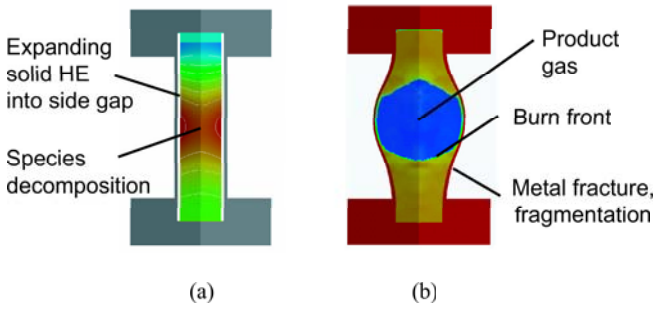

FIG. 2: (a) Pre-ignition characterized by slow thermo-chemical decomposition of HE. (b) Post-ignition illustrated with rapid burn propagation due to expanding hot product gases.

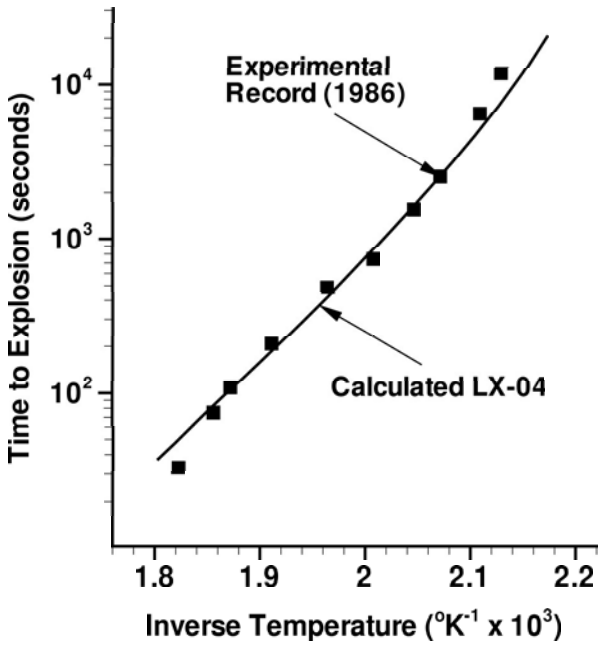

FIG. 3: Experimental and calculated ODTX times to thermal explosion versus inverse temperature for LX-04.

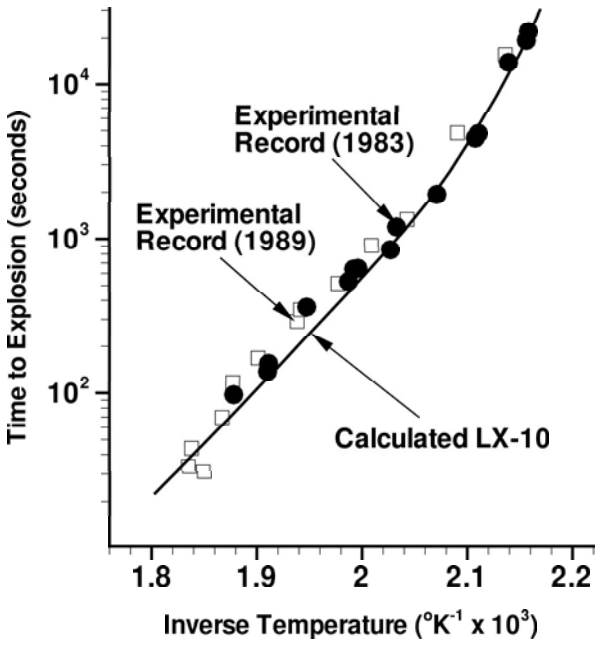

FIG. 4: Experimental and calculated ODTX times to thermal explosion versus inverse temperature for LX-10.

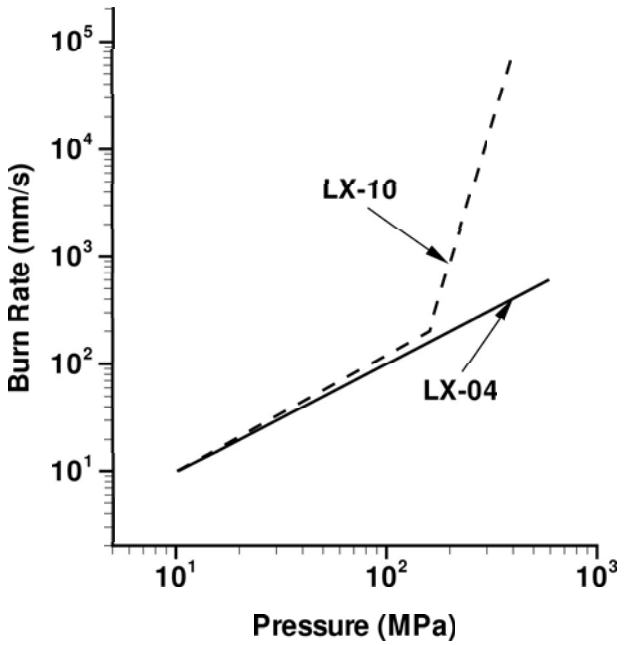

FIG. 5: Curve fits of the measured rate of deflagration for both HE's based on experiments in [28].

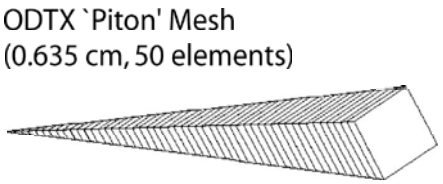

FIG. 6: One-dimensional (spherical symmetry) mesh used in the ODTX simulations.

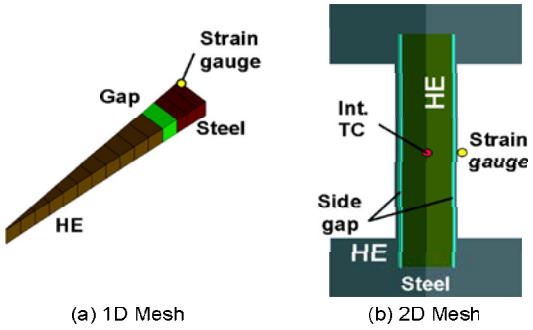

FIG. 7: Meshes used in the STEX simulation. The 1D mesh is generated from a slice along the center radial line of the 2D mesh on the right. The steel wall thickness is 0.4 cm for LX-04, and 0.3 cm for LX-10 (not shown). In both, there exists a 7% gap (by volume) in LX-04 system while a 8.66% gap is present in the LX-10 system.

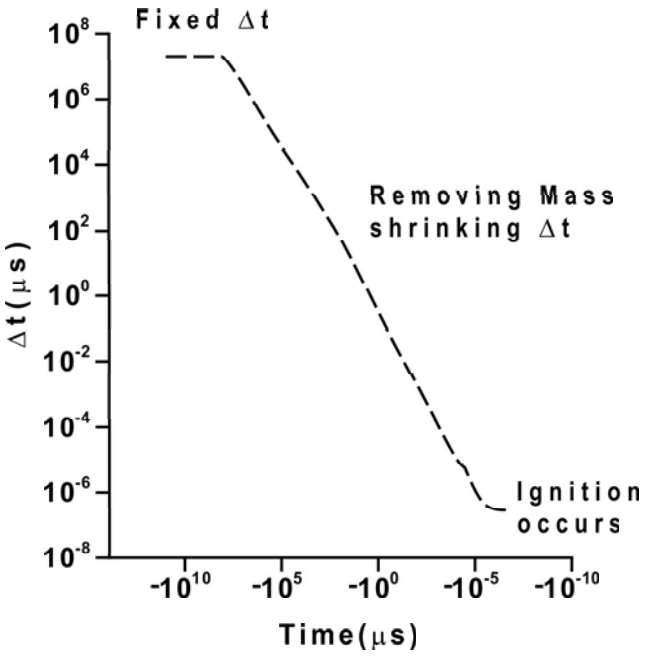

FIG. 8: History of the time-step size during the final hours of thermal explosion. Shown from 3 hours prior to ignition at time $t \approx 10^{-7}$ μs.

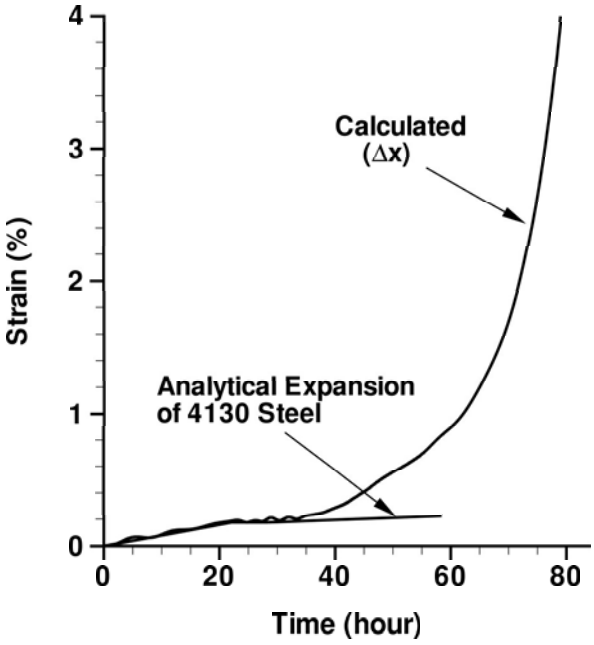

FIG. 9: Simulated mechanical response of confined LX-04 in a 1D STEX model. The wall hoop strain is at location no. 2 in Fig. 7(a). The strain calculation agrees with the empty vessel result until about 35 hours as chemical decomposition of HE becomes pronounced in the confined system.

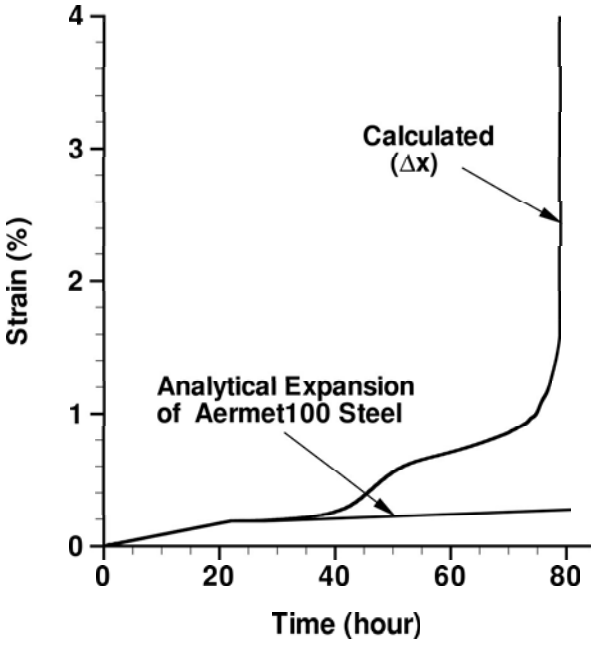

FIG. 10: Simulated mechanical response of confined LX-10 in a 1D STEX model. The wall hoop strain is at location no. 2 in Fig. 7(a). The strain calculation agrees with the empty vessel result until about 35 hours as chemical decomposition of HE becomes pronounced in the confined system.

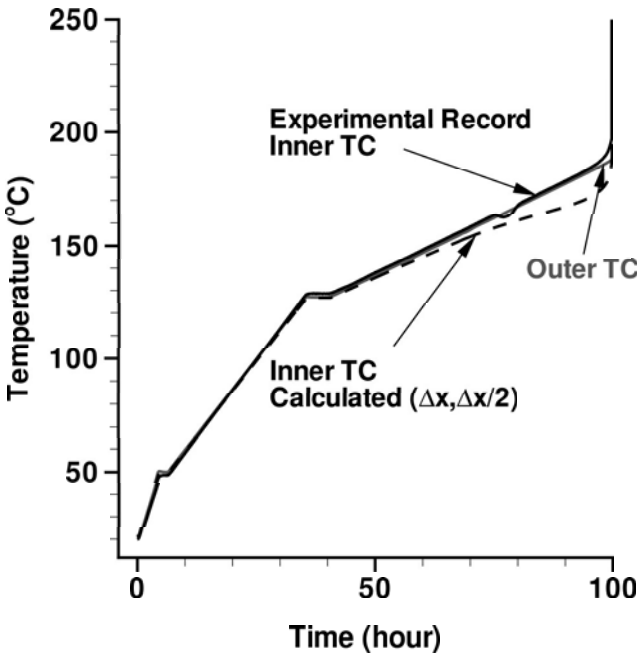

FIG. 11: Calculated thermal response of confined LX-04 in a 2D STEX experiment. The control and internal thermocouples are located at positions nos. 1 and 6 in Fig. 1(b), respectively. The predicted ignition temperature is approximately 1 degree lower than the STEX result. Δx mesh is used.

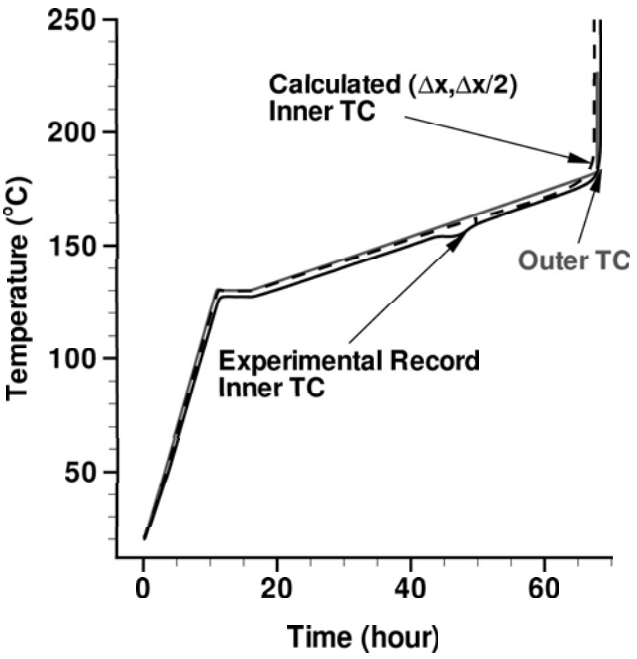

FIG. 12: Calculated thermal response of confined LX-10 in a 2D STEX experiment. The control and internal thermocouples are located at positions nos. 1 and 6 in Fig. 1(b), respectively. The predicted ignition temperature is less than a degrees off from the measurement. Δx mesh is used.

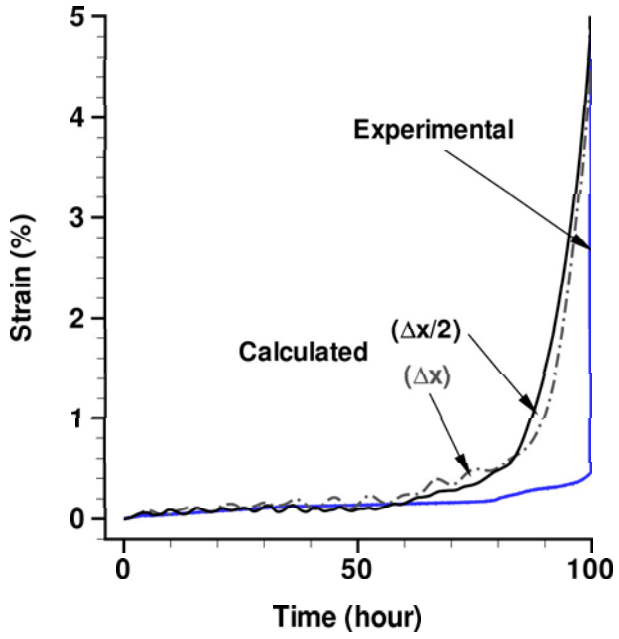

FIG. 13: Experimental and calculated hoop strain records from the slow heating to the thermal runaway phase for LX-04.

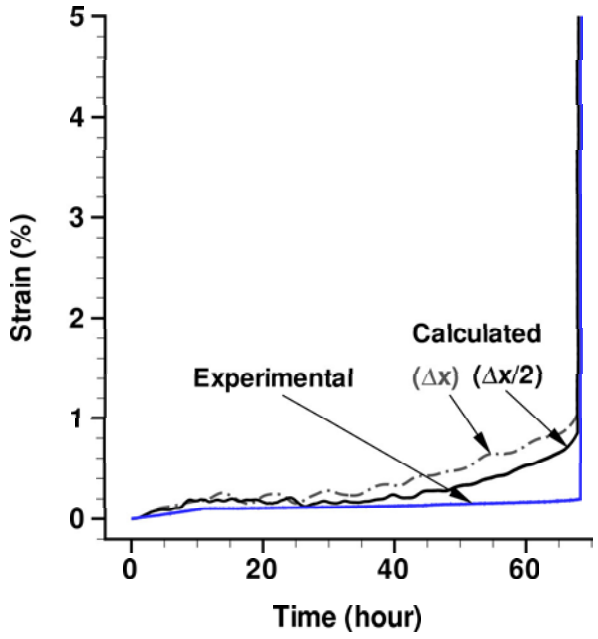

FIG. 14: Experimental and calculated hoop strain records from the slow heating to the thermal runaway phase for LX-10.